Synchrotron X-ray computed microtomography study on gas hydrate decomposition in a sedimentary matrix

Yang, Lei ; Falenty, Andrzej ; Chaouachi, Marwen ; Haberthür, David ; Kuhs, Werner F

DOI: https://doi.org/10.1002/2016GC006521

AGU PUBLICATIONS

Geochemistry, Geophysics, Geosystems

RESEARCH ARTICLE
10.1002/2016GC006521

Synchrotron X-ray computed microtomography study on gas hydrate decomposition in a sedimentary matrix

Lei Yang[1,2], Andrzej Falenty[2], Marwen Chaouachi[2], David Haberthür[3], and Werner F. Kuhs[2]

[1]Key Laboratory of Ocean Energy Utilization and Energy Conservation of Ministry of Education, Dalian University of Technology, Dalian, China, [2]GZG, Abt. Kristallographie, Georg-August-Universität Göttingen, Göttingen, Germany, [3]X-ray Tomography Group, Swiss Light Source, Paul Scherrer Institute, Villigen, Switzerland

Key Points:
- Time resolved, microstructural aspects of pressure-induced gas hydrate dissolution in sediments followed with in situ synchrotron tomography
- A diffusion-limit on the liberated gas transport through the gas-enriched water and a resulting gas concentration gradient is indicated
- Possible effects of the microstructural behavior of hydrate decomposition on mechanical stability and permeability properties are discussed

Supporting Information:
- Supporting Information S1

Correspondence to:
W. F. Kuhs,
wkuhs1@gwdg.de

Citation:
Yang, L., A. Falenty, M. Chaouachi, D. Haberthür, and W. F. Kuhs (2016), Synchrotron X-ray computed microtomography study on gas hydrate decomposition in a sedimentary matrix, *Geochem. Geophys. Geosyst.*, *17*, 3717–3732, doi:10.1002/2016GC006521.

Received 8 JUL 2016
Accepted 25 AUG 2016
Accepted article online 29 AUG 2016
Published online 15 SEP 2016

ABSTRACT *In-situ* synchrotron X-ray computed microtomography with sub-micrometer voxel size was used to study the decomposition of gas hydrates in a sedimentary matrix. Xenon-hydrate was used instead of methane hydrate to enhance the absorption contrast. The microstructural features of the decomposition process were elucidated indicating that the decomposition starts at the hydrate-gas interface; it does not proceed at the contacts with quartz grains. Melt water accumulates at retreating hydrate surface. The decomposition is not homogeneous and the decomposition rates depend on the distance of the hydrate surface to the gas phase indicating a diffusion-limitation of the gas transport through the water phase. Gas is found to be metastably enriched in the water phase with a concentration decreasing away from the hydrate-water interface. The initial decomposition process facilitates redistribution of fluid phases in the pore space and local reformation of gas hydrates. The observations allow also rationalizing earlier conjectures from experiments with low spatial resolutions and suggest that the hydrate-sediment assemblies remain intact until the hydrate spacers between sediment grains finally collapse; possible effects on mechanical stability and permeability are discussed. The resulting time resolved characteristics of gas hydrate decomposition and the influence of melt water on the reaction rate are of importance for a suggested gas recovery from marine sediments by depressurization.

1. Introduction

Gas hydrates (GHs) are crystalline inclusion compounds, in which hydrogen-bonded water molecules form a framework of cages, capturing gas molecules inside [*Sloan and Koh*, 2007]. Their potential as a future energy resource, hypothetical impact on global climate, threat to transportation of hydrocarbons in pipelines as well as their considerable capacity for gas storage have made these materials an object of intense research worldwide [*Chong et al*., 2016; *Falenty et al*., 2014; *Koh et al*., 2010; *Krey et al*., 2009]. Commercial gas recovery from natural reservoirs of GHs requires a detailed knowledge on GH decomposition characteristics in sedimentary matrices which largely depend on the concentration and the actual fabrics of GHs within the sediments. Phase changes of solid hydrates into gas/water during decomposition and the concomitant rise of pore pressure may significantly impact the overall mechanical properties of the sea bed and could well lead to slope instabilities [*Dillon et al*., 2001; *Pauli et al*., 2000]. Consequently, numerous lab-scale studies on GH decomposition in sedimentary matrices have been conducted in order to prepare for safe and efficient field production tests. The decomposition of hydrates in sedimentary matrices is a complex process involving phase transitions, heat transfer, and gas/water permeation [*Ye and Liu*, 2012]. Typically the decomposition process is evaluated based on the overall gas production rate and little detailed information is available due to the limitations in detecting the local hydrate evolution inside bulky pressure cells [*Haligva et al*., 2010; *Li et al*., 2012b; *Linga et al*., 2009]. Based on the variation of gas production rates the decomposition process was found to be nonuniform with time, with pressure reduction governing the fast free gas release stage, remaining sensible heat dominating the decomposed-gas recovery stage, and ambient heat conduction forcing the final low-rate gas production stage [*Li et al*., 2012b; *Zhao et al*., 2015]. A reformation process of hydrates was also suggested to occur during gas production inside a bulk vessel as deduced from temperature anomalies, which were declared to result from an insufficient supply of sensible heat [*Zhao et al*., 2015]. The frequently inhomogeneous nature of the decomposition process was largely ascribed to the local build-up of differential pressures and heat [*Li et al*., 2012b; *Zhao et al*., 2015]. However, neither of these

studies provided details on the microstructural evolution of hydrates in pore spaces, which are ultimately necessary to confirm these findings.

Quartz or silica sands with grain diameters ranging from 100 to 630 μm were most widely employed as equivalent for natural sedimentary porous matrices [*Kono et al*., 2002; *Li et al*., 2012a, 2012b; *Linga et al*., 2009; *Tang et al*., 2007; *Zhao et al*., 2015]. Hydrate decomposition was found to be completed faster in finer silica sands, indicating a grain-size-dependent behavior, which was attributed to lower initial hydrate saturations in finer grain sediments [*Liu et al*., 2008]. Nevertheless, the porosity, permeability, and pore-scale gas/water redistribution during hydrate decomposition could also exert a significant influence on gas production rate. In fact, the distribution pattern of GHs in pore spaces was found to have a crucial impact on permeability of hydrate-bearing sediments, which will directly influence the gas and water release process [*Kleinberg et al*., 2003]. Yet the time-dependent microstructural characteristics of GHs in pore spaces during decomposition are still largely unclear.

Efforts have also been made toward larger field-scale. Extensive numerical work on the gas production potential of various hydrate accumulations has been conducted based on the actual geological and oceanographic data in Mallik site of Canada, Nankai Trough of Japan, and Alaska North Slope of USA [*Anderson et al*., 2011; *Konno et al*., 2010a; *Moridis*, 2004; *Moridis et al*., 2004]. An effective permeability of hydrate-bearing sediments higher than a threshold value was considered crucially necessary for depressurization-induced gas production from marine hydrate reservoirs [*Konno et al*., 2010b]. Moreover, extremely high local pressure at the decomposition front would possibly result in fracturing of the hydrate-sediment for cases of low permeability due to the loss of sediments strength [*Pauli et al*., 2003; *Tsimpanogiannis and Lichtner*, 2007]. The secant modulus was measured to drop by 42.6% after hydrate decomposing for 48 h, indicating a distinct difference in mechanical properties of hydrate-bearing sediments after hydrate decomposition, which might be a potential inducement of slope instability [*Song et al*., 2014]. The abovementioned studies have provided a first understanding of overall gas production behavior on both lab-scale and field-scale. However, plenty of challenges and open issues still remain; of particular interest is the role of the initial distribution patterns of hydrates in natural sands and the changing geomechanical and reservoir/well stability [*Moridis*, 2011]. Moreover, the majority of reservoir gas production simulations are unable to take the microstructural evolution of GHs during gas production into account; instead a series of assumptions are usually made including the homogeneous distribution of GHs in pores, a parallel heat flow through fluids and solids, the neglect of water movement, and a constant permeability [*Ji et al*., 2001; *Xu and Ruppel*, 1999].

Consequently, attempts have been made to provide insight into hydrate decomposition process (natural or synthesized) through various visualization techniques across a range of scales of hydrate accumulations from large field-scale [*Collett*, 1999; *Hyndman et al*., 1999], laboratory pilot-scale (over 100 l vessel volume) [*Li et al*., 2012b; *Wang et al*., 2016], core-scale (usually cylindrical samples with diameter of less than 10 cm) [*Baldwin et al*., 2003; *Gao et al*., 2005], to pore-scale (pores down to several microns) [*Tohidi et al*., 2001]. The most rudimentary form of visualization is a 2-D or even 3-D profiling with thermocouples distributed inside large pressure vessels [*Li et al*., 2012b; *Wang et al*., 2016] that directly illustrate the location-dependent differential temperature resulting from the complex heat transfer process during hydrate decomposition, albeit with quite coarse resolutions. Studies on core-scale decomposition characteristics of hydrates have been reported; decomposition of tetrahydrofuran (THF) hydrates through raising temperature followed with magnetic resonance imaging (MRI) showed melting at the water-hydrate interface even though the temperature distribution in solid hydrate phase was uniform, which indicated an inhomogeneous nature of decomposition [*Gao et al*., 2005]. A structured layer with semi-clathrate organizations was hypothesized to exist at the decomposing interface, where hydrates preferentially decayed [*Gao et al*., 2005]; another explanation is that hydrates isolated from the liquid phase were found more difficult to decompose requiring higher temperature [*Tohidi et al*., 2000]. Likewise, a radially shrinking decomposition pattern initiated at outer edge of the cylinder-shaped sample was also observed [*Baldwin et al*., 2003]. But there is no gas phase involved for THF system; therefore it is at least questionable if THF formation/decomposition is comparable to GHs. In any case, observation at a scale of several hundred microns or even smaller is still beyond the resolution of MRI technique. Methane gas release from hydrate decomposition was also observed with high-resolution optical microscopy, which offered some information on 2-D gas/water rearrangements during hydrate decomposition [*Katsuki et al*., 2008]. *In-situ* Raman spectroscopy was found helpful in observing the decomposition of hydrates by providing time-resolved spectra for CH_4 molecules encaged in hydrate cavities during hydrate decomposition [*Komai et al*., 2004; *Liu et al*., 2008], but powerless in illustrating

detailed morphological characteristics of decomposing hydrates in pores. Cryo scanning electron microscopy (cryo-SEM) allows a more detailed access of surface properties down to the nanometer scale on recovered samples, which has been extremely useful for the observation of GHs and ice surfaces [*Falenty et al*., 2014; *Kuhs et al*., 2000]. Nevertheless, this method is limited by the difficulty of separating ice and hydrates in frozen state and possible artifacts arising during the recovery and quench. Similar problems were encountered in observations on cryo-preserved GH samples recovered from the seafloor *via* synchrotron X-ray tomographic microscopy [*Klapp et al*., 2012; *Murshed et al*., 2008]. Attempts to observe hydrate decomposition were also made through X-ray computed tomography (X-CT). Inhomogeneous decomposition patterns with the dissociating front moving radially inward from the vessel wall were observed, which was attributed to the thermally dominated decomposition after instant depressurization and the heat transfer through the vessel wall [*Kneafsey et al*., 2007]. In a combination of X-ray tomographic imaging and acoustic signal measurements [*Waite et al*., 2008], a nonuniform hydrate redistribution resulting from water migration after a depressurization and subsequent repressurization process was observed and its effect on acoustic properties of hydrate-bearing quartz sands was investigated; this study suggests significant effects of gas/water/hydrate rearrangements during decomposition on the physical characteristics of porous matrices containing GHs. Yet insufficient spatial resolution did not allow following the pore-scale microstructural evolution of GH decomposition and its possible links to changes in bulk properties. This limitation has been overcome only recently with a synchrotron X-ray tomographic study of GH formation in sedimentary matrices [*Chaouachi et al*., 2015; *Sell et al*., 2016]. Sub-micrometer resolution imaging allowed for the first time for an unequivocal identification of a fluid phase film with the thickness of up to several microns between hydrates and the surfaces of quartz grains [*Chaouachi et al*., 2015]. In this study some preliminary observations of hydrate decomposition at the pore scale were also made. Here we extend this *in-situ* time-resolved study on the decomposition characteristics of GHs in sedimentary matrices. Special attentions are placed on the microstructural evolution during GH decomposition, on local decomposition rates as well as on the fate of released gas and melt water during decomposition. The sub-μm pixel size observations are expected to have implications for the understanding of the decomposition mechanism and its effect on physical properties during gas recovery from natural hydrate reservoirs, but may also shed some light onto GH decomposition processes in applications from chemical engineering.

2. Experimental

The formation and decomposition of GHs were investigated *in-situ* through high-resolution synchrotron radiation X-ray tomography (SRXCT) at the TOMCAT beamline, Swiss Light Source (SLS), Paul Scherrer Institute (PSI) in Villigen (Switzerland) [*Marone and Stampanoni*, 2012; *Stampanoni et al*., 2006]. With high brilliance, a flexible selection of the energy window and exceptional optics for sub-micrometer pixel sizes (down to 350 nm in full-field geometry) this beamline is particularly well adapted to follow dynamic processes *in-situ* in complex environmental cells. For the experiments presented here the X-ray beam energy was set to 21.9 keV to assure the optimal tradeoff between attenuation and data collection time. After penetrating the sample, X-rays are converted into visible light by a 20 μm thick LuAG:Ce scintillator, tenfold enlarged with an optical objective (UPLAPO10x) and digitized by a high-resolution CCD camera (2560 $\times$ 2160 pixels). Each acquired tomogram consists of 3201 individual projections collected over 180° in under 12 min. The data were reconstructed by a gridded Fourier transform-based algorithm [*Henke et al*., 1993; *Shulakova et al*., 2013] which yields an image matrix of 2560 $\times$ 2560$\times$2160 voxels. With a resulting isometric voxel size of 0.65 μm it is possible to resolve fine microstructural details at interfaces between gas, water, sediment grains and hydrate. To enhance density contrast differences between these phases methane gas has been substituted with xenon, known to be similar with respect to solubility and diffusivity as well as physical properties of the resulting GHs [*Chaouachi et al*., 2015]. The substitution also allows for more modest formation conditions of merely $\sim$0.4 MPa at T=276 K that alleviate potential hazards of operating under high pressures with explosive gas, a serious concern at large scale research facilities (e.g., synchrotrons, reactors, spallation sources etc.). Data used to establish compositional gradients in water films were additionally enhanced with a simultaneous phase and amplitude extraction algorithm (phase-retrieval) [*Paganin et al*., 2002] which for some loss of resolution improves the dynamic range of reconstructed projections.

GHs for decomposition experiments were prepared *in-situ* from a mixture of fine frost particles and natural quartz sand (200–300 μm) from Lyubertsy (Moscow region, Russia) [*Chuvilin et al*., 2011]. The frost was prepared with pure water instead of sea water, due to the concern that hydrate formation from salty water will

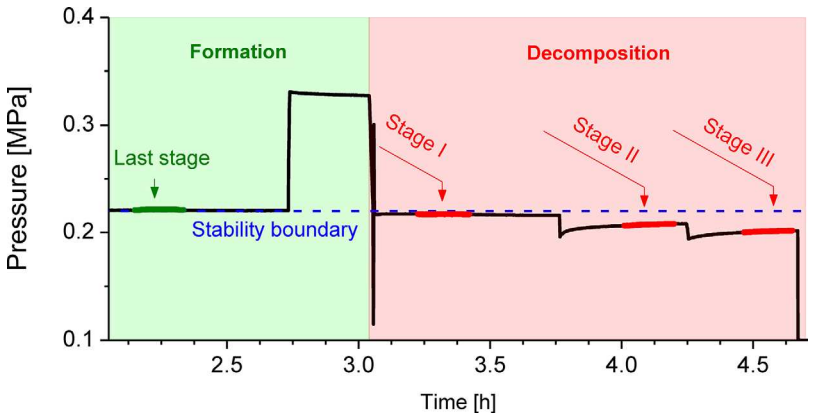

Figure 1. The stop-and-go procedure for the in situ formation and decomposition of Xe-hydrate. Green/Red sections mark the duration of individual tomographic scans.

likely lead locally to the generation of artificially highly concentrated brine, thereby introducing possible disturbances to the measured X-ray contrast. The presence of sea water in the system or its absence (pure water) would not have a pivotal influence on the presented findings. A portion of the homogenized starting material was loaded and compacted under liq. N_2 into an aluminum sample holder that was later mounted at the base of a custom built pressure cell [*Chaouachi et al*., 2015]. After sealing the setup with a TECAPEI (Polyetherimide) dome, the ambient atmosphere surrounding the sample was purged *via* several compression and decompression cycles with pure Xe gas while staying below the thermodynamic stability boundary of Xe-hydrate. The pressure inside the cell was logged with an ASHCROFT KXD pressure sensor every 5 s. During the thermal equilibration toward the chosen experimental conditions frost transforms to juvenile water that fills on average ∼17 vol.% of pore spaces [*Chaouachi et al*., 2015]. The temperature of the sample is actively regulated within ± 0.1 deg. *via* a PID controlled Peltier element at the base of the setup. After reaching a constant temperature of 276 K the Xe pressure was increased to 0.4 MPa to transform pore water into Xe-hydrates. The formation process was followed in a series of steps with the so-called "stop-and-go" *in-situ* tomography [*Chaouachi et al*., 2015; *Falenty et al*., 2015]. With this approach the ongoing reaction is periodically paused by a rapid decrease of pressure from the formation conditions (∼0.33 MPa) down to the stability boundary (0.22 MPa). In this equilibrium state tomography scans can be taken on the essentially static system. The further reaction is triggered by a subsequent repressurization to the formation conditions. The procedure is repeated several times to capture consecutive stages of the formation until nearly a full conversion where no fast uptake of Xe gas is observed. Further on, the sample was repressurized for the last time and kept at the formation conditions (0.33 MPa) for ∼20 min in attempt to convert minute amount of rest water before the decomposition cycles began [*Chaouachi et al*., 2015].

The decomposition of the *in-situ* grown GHs formed with the above procedure was followed in three stages. In the first step aiming for the initial surface destruction the pressure was rapidly dropped to ambient atmosphere and repressurized to the stability boundary within 10 s. After a period of stabilization the first tomogram was taken. In the second decomposition step the pressure was rapidly reduced from the stability limit to ∼0.195 MPa. Immediately after closing the system the pressure quickly increased due to the rapid decomposition. After several minutes the reaction slowed down as it was approaching the stability boundary and a tomogram could be taken. Even if not fully equilibrated, changes to GH microstructures at this stage are small enough not to affect the quality of the reconstructions. The same procedure was repeated for the final, third stage; the pressure-time protocol followed is shown in Figure 1.

3. Results

3.1. Microstructural Setting Resulting From the Formation Process

At the final stage of the formation the majority of free water is found to be transformed into polycrystalline hydrate accumulations unevenly distributed in the sedimentary matrix (see Figure 2). Such inhomogeneous distributions of GHs are repeatedly reported in numerous studies investigating GH formation in fully and partially

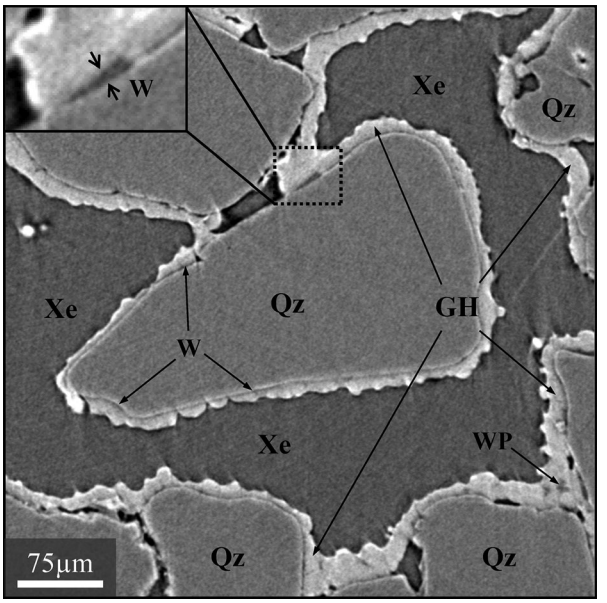

Figure 2. CT image illustrating the final state after the full formation process. Clathrates crystals are primarily organized in films enveloping quartz grains. A thin water layer (W) remains between gas hydrates (GH, white) and quartz sands (Qz, light gray). The growth of GH crystals entraps small volumes of formation water to form a water pocket (WP); this water was found to be enriched in Xe gas [*Chaouachi et al.*, 2015]. Xe gas (Xe) is shown in gray.

water saturated sedimentary matrices on scales from a few μm to several cm; they are usually ascribed to the nature of the GH nucleation and the locally varying p-T conditions. In the partially water saturated systems the location of GH accumulations can be additionally affected by the initial water distribution and its displacement during the pressurization as we observed in our recent work [*Chaouachi et al.*, 2015]. From this work the average size of freshly formed clathrate crystals appears to be a few μm but some of the crystals can reach 10–20 μm. This broad distribution is well recognizable in the uneven morphology of GH masses where larger, nearly isometric crystals protrude into pore spaces from accumulations of smaller ones.

In particular for lower water concentrations clathrate crystals are predominantly organized in layers enveloping quartz grains (see Figure 2); the contact is mediated by a layer of water up to a μm thick that can be best identified at grain boundaries between individual polyhedral crystals of GHs [*Chaouachi et al.*, 2015]. The presence of such a water film is likely to be an intrinsic property of quartz-GH interfaces and has been already inferred in early light microscopic investigations [*Tohidi et al.*, 2001] and predicted by several computer simulations [*Bagherzadeh et al.*, 2012; *Bai et al.*, 2011; *Liang et al.*, 2011]. In frame of the Hamaker approach this residual water can be seen as a consequence of molecular interactions between quartz and clathrate that favor a transitional disordered, liquid layer over a direct contact [*Bonnefoy et al.*, 2005]. Following this argumentation, the chemical activity of gas molecules in this water film is likely to approach that of GHs but due to molecular interactions the crystallization is inhibited. At near equilibrium conditions with their continuous formation-dissolution cycles at the clathrates interface water is expected to be supersaturated in gas molecules. They can either remain metastably dissolved in the liquid by a cooperative loss of long-range order resembling a dislocation saturated crystal [*Poirier*, 2000] or form nm size bubbles [*Liang et al.*, 2011; *Smirnov and Stegailov*, 2012; *Yagasaki et al.*, 2014] as a consequence of the high entropic cost of the hydrophobic hydration leading to hydrophobic assembly [*Chandler*, 2005]; it may well be that the initial single-molecule hydrophobic hydration is rapidly followed by the nucleation of nm size bubbles. In any case, a molecular picture of this gas-enriched water cannot be drawn from our experimental data [*Chaouachi et al.*, 2015]. Within the resolution of our experiment, all conceivable enrichment scenarios will provide a comparable effect of increased absorption (i.e., changes in the gray values for water phase) in comparison to the gas-free liquid.

Clathrate crystals are also found to agglomerate in porous structures that fill voids between quartz grains (see Figure 2). Pores of such accumulations are predominantly filled with gas but in some places the growth of GH crystals entraps small volumes of formation water. In contrary to interfacial water at the boundaries to quartz, these inclusions will eventually transform fully into GHs; yet due to a sluggish diffusive transport of guest molecules across clathrate cages [*Salamatin et al.*, 2015] the complete conversion would exceed the time limitation imposed by the experiment. This is confirmed in our scans where in spite of the repressurization before the decomposition series most of these inclusions can be found also in the first decomposition step. Indeed, gray values measured in these inclusions also suggest a supersaturation with gas of water contained in pockets surrounded by clathrates [*Chaouachi et al.*, 2015].

3.2. Microstructural Features of Decomposition and Decomposition Rates

Our submicron pixel size tomographic experiments allow a detailed microstructural identification of the decomposition features and the overall GH decomposition rates. Clearly, the decomposition process is

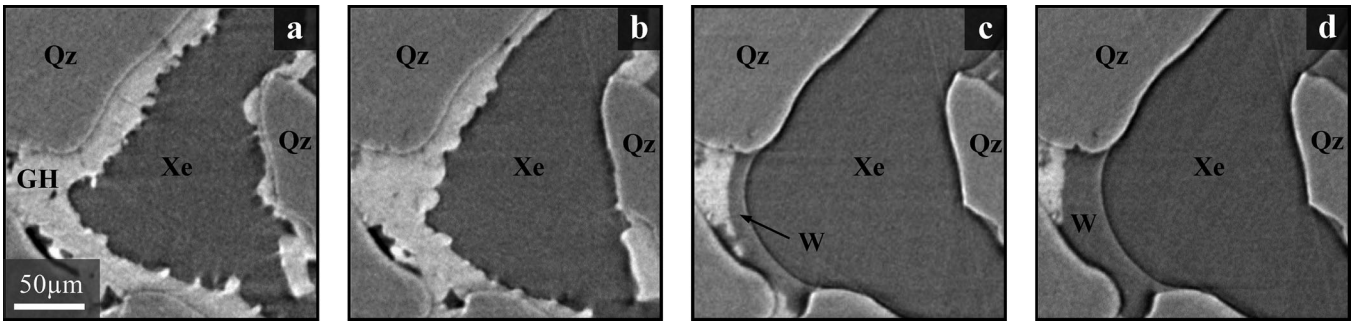

Figure 3. GH decomposition in pores as a function of time. t_R represents the reaction time. (a) Full formation, (b) t_R=10 s, (c) t_R= 20.37 min, (d) t_R=37.87 min. The decomposition is initiated at the gas-hydrate interface, and polyhedral crystals protruding from the gas hydrate (GH, white) surface will preferentially decompose to form a smooth interface in the first 10s of decomposition (stage I, see Figure 3b). Hardly any mobile water (W, gray) is visible in this stage. Hydrate in the vicinity of quartz sands (Qz, light gray) remains largely unchanged. The water produced from decomposition then gradually wets pore spaces enveloping residual hydrates inside after hydrate decomposing for 20.37 min (stage II, see Figure 3c). The following decomposition takes place at the hydrate-water interface, with hydrate patch ablating toward the narrow grain contacts. Concomitantly the water film thickens over time (stage II and III, see Figures 3c and 3d). Xe gas (Xe) is shown in gray.

initiated at the clathrates-gas interface with polyhedral single crystals protruding into the gas phase preferentially decomposed smoothening the hydrate-gas interface (see Figures 3a and 3b). On further decomposition a water layer accumulates at the hydrate surface separating clathrates from the gas phase. The subsequent decomposition still takes place at the hydrate surface (see Figures 3c and 3d) and is likely limited by the gas out-diffusion into the bulk gas phase through a gradually thickening water layer. These observations are in agreement with earlier views that the decomposition starts with a breakdown of the clathrate surface, followed by a release of guest molecules into the surrounding liquid water [*Kim et al*., 1987]. It is noteworthy that the contacts of GH with the quartz grains remain unchanged until the decomposition front reaches this interface from the hydrate side, i.e., until the very end of the decomposition process (see supporting information Figure S1); this scenario with the hydrate spacers remaining largely intact will enhance the mechanical strength of the sediments until the final collapse (see supporting information Figure S1).

The density contrast between Xe hydrates and other components is sufficiently large to open the full access to spatial features of the hydrate phase *via* a gray scale threshold method in ImageJ [*Abràmoff et al*., 2004; *Promentilla and Sugiyama*, 2010] (see supporting information Figure S2). The decomposition rate is then obtained through the area/volume of the decomposed hydrates and the duration of decomposition. The decomposition process in our experiment is completed in a time span of about half an hour of which the initial microstructures and three decomposition stages were captured by tomographic imaging. Note that the decomposition proceeds with locally varying rates even in each single stage, so the decomposition rates provided here are average rates. In stage I they range from 34.79 to 227.82%/min (the relative decomposition rate is defined as the ratio of the absolute rate to the hydrate area/volume before decomposition, and the rate over 100% indicates that hydrates will be completely decomposed within 1 min), with the global decomposition rate of 107.06%/min; hydrates in stage II decompose distinctly slower, with the rates ranging from 2.08 to 4.13%/min and the global rate of 2.48%/min; the rates in the stage III decline to 0.07–0.78%/min with an average global rate of 0.60%/min (see Table S1). The decomposition rate, irrespective of area and volume, shows a dependence on reaction time; in other words, hydrates decompose the fastest when decomposition is initiated, and then decelerate with time. This is in accordance with a 3-D simulation of hydrate decomposition based on Kim-Bishnoi intrinsic kinetic models [*Sun and Mohanty*, 2006], and an experimental study on gas production behavior by depressurization [*Haligva et al*., 2010]. But in our case, the sharper pressure drop in the beginning stage than the following stages and the corresponding larger difference in the fugacity of gases at equilibrium pressure and decomposing pressure are also responsible for the initially faster decomposition. If the water layers formed at the hydrate surface remain largely unperturbed during decomposition, the escape of liberated gas molecules into the bulk gas phase should be limited primarily by the solubility and diffusivity of xenon in water; the equilibrium values are 1.6×10^{-4} mg L^{-1} at 276 K for the solubility and 9.3×10^{-6} cm^2 s^{-1} at 283 K for the diffusivity of Xe gas in water [*Haynes*, 2014]. Yet gray values measured in water appears to indicate an anomalously high enrichment of gas in the liquid [*Chaouachi et al*., 2015]; the diffusivity for xenon in such supersaturated water has never been established and merits further considerations. Since the difference in chemical potentials defines the intrinsic

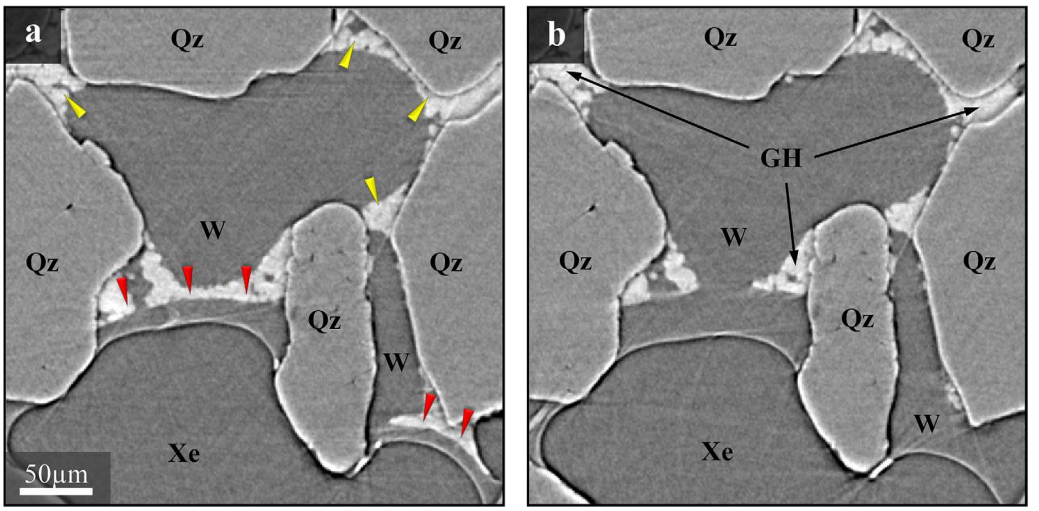

Figure 4. Local tomograms showing the diffusion limitation effect of water on hydrate decomposition. (a) t_R= 20.37 min, (b) t_R=37.87 min. Gas hydrate (GH, white) patches closer to the gas-water interface (see red arrows) decompose more readily than those further away (see yellow arrows), due to the shorter pathway for gas to diffuse into the bulk gas phase. Quartz sands (Qz) are shown in light gray, Xe gas (Xe) and water (W) in gray.

driving force for the decomposition we expect that a high chemical activity of xenon at the decomposing hydrate-water boundary slows down further desorption of gas out of the clathrates' interface. Concentration gradients will lead to a diffusive flow of xenon toward the water-gas interface. As a result, hydrate patches closer to the gas-water interface are more likely to decompose than those further away due to the shorter gas diffusion pathways through the water phase (see Figure 4). Moreover, the pressure was found to bounce back to the stability boundary rather slowly at the end of stage II and III (see Figure 1), which further corroborates the diffusion limited escape of gas from melting hydrate across the water layer with a resulting slowly decreasing driving force for decomposition. Our results provide strong evidence for a rate-limiting role of the water layer located between hydrates and free gas; the permeation limitation of any gas produced during decomposition is enhanced with increasing thickness of the water layer, which explains the deceleration of the decomposition reaction with time. This two stage character of the decomposition appears to be formally analogous to the 2-stage processes during GH formation on ice spheres, where a first rapid hydrate film formation on the surface is followed by an increasingly slowing down transformation, due to a diffusion-limited transport of gas through the growing hydrate phase [*Falenty et al*., 2013; *Salamatin et al*., 2015]. Attempts have been made on the mass transfer mechanism during hydrate decomposition, and tube structures were suggested to connect decomposing and well-preserved hydrate patches as a pathway of degassing [*Klapp et al*., 2012]. However, the *ex-situ* processing of the sample with liquid nitrogen overshadows this mass transfer regime. A numerical study on gas production from hydrate accumulations through depressurization also indicates the negative effect of water production on gas production rate [*Moridis et al*., 2004], yet without any specific microstructural evidence. The decomposition rates in the first stage also show a spatial inhomogeneity along the vertical direction of the sample. Hydrates closer to the top appear more likely to decompose faster (see Table S1). This possibly arises from the lower hydrate saturation and the resulting higher permeability in upper sections of the cylindrical sample, which both help the out-diffusion of liberated gas. In the following stages, the gas-diffusion-limited decomposition is clearly governed by water production and redistribution. The established decomposition rates together with our submicron observations should provide good guidance to understand the kinetics of GH decomposition in porous matrices in general - in particular for a depressurization-induced gas recovery from marine sediments, where an analogous scenario with water layer acting as a diffusion barrier decelerating the decomposition should be expected as well.

3.3. Water Production and Redistribution

In the course of the initial decomposition process, hardly any mobile water is visible (see Figure 3b). The water produced from hydrate decomposition is either trapped within the hydrate patch as a water pocket (WP) replacing gas pores (see supporting information Figure S1), or involved in the secondary hydrate

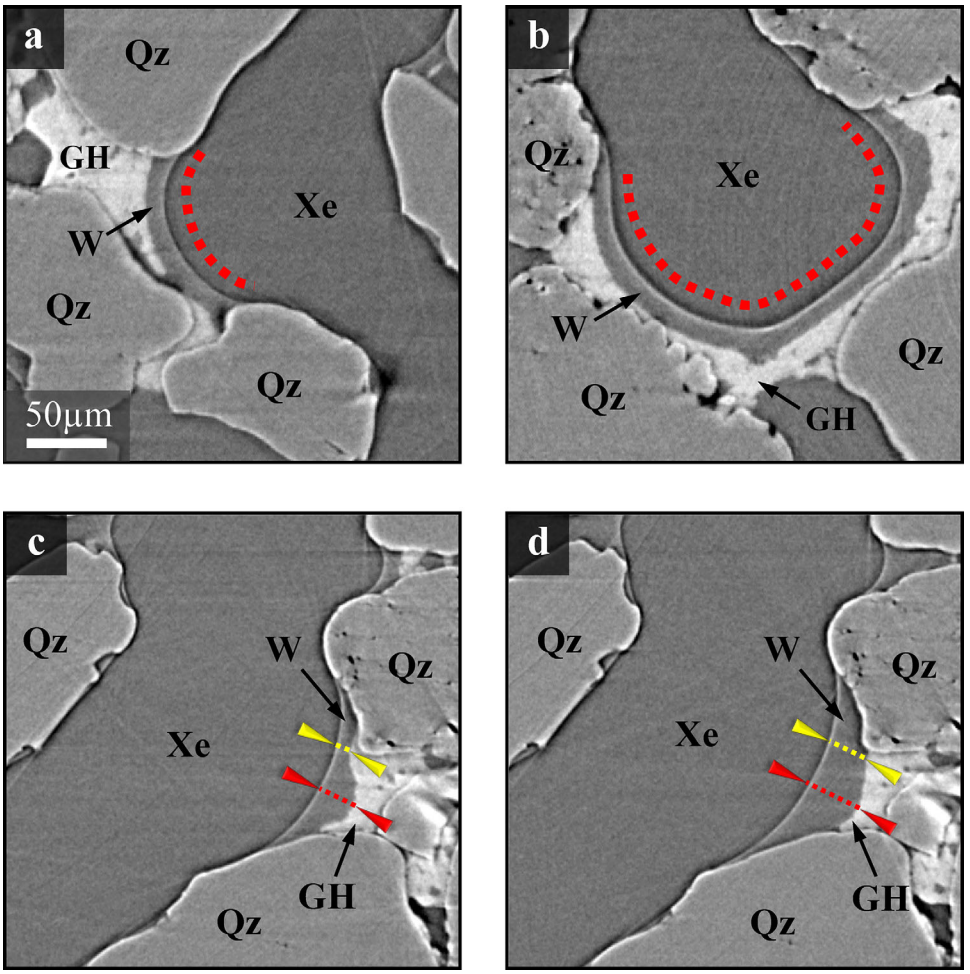

Figure 5. (a, b) t_R= 20.37 min. The decomposing front of gas hydrate (GH, white) mirrors the shape of neighboring water-gas boundaries; Red dotted lines are drawn parallel to the interface as a guide to the eye. (c) t_R= 20.37 min, (d) t_R=37.87 min. Thicker water layers (W, gray, see red arrow) clearly lead to a slower decomposition process of the underlying GHs (which in turn slows down the increase of water layer thickness with time); conversely, thinner water layers (see yellow arrow) contribute to a faster decomposition of hydrates and an increase of local water layer thickness. Quartz sands (Qz) are shown in light gray, Xe gas (Xe) in gray.

formation process (discussed in chapter 3.5). The formation of WPs is mainly attributed to the porous structure and the predominantly hydrophilic character of the GH phase [*Chaouachi et al*., 2015; *Hirata and Mori*, 1998] coupled with capillary forces, which drive water formed at the hydrate-gas interface inside hydrate patches. The gas release and locally inhomogeneous heat distribution also play some role in water migration, but due to the minute volume of melt water generated at this stage a more precise influence of these parameters could not be evaluated. A similar behavior that nearly no water is produced in the first moments of hydrate decomposition has been reported as well [*Li et al*., 2011]. Our observations allow tracing back the fate of melt water, supersaturated in Xe gas, which gradually invades pore spaces. By the end of stage II of hydrate decomposition residual hydrates are nearly fully immersed in the melt water (see Figure 3c) with only a few gas filled pores remaining within hydrate patches. The hydrate decomposition front tends to mirror the shape of neighboring water-gas boundaries, forming meniscus-shaped water layers with a fairly uniform thickness between hydrates and gas phase at the end of stage II of decomposition (see Figures 5a and 5b). If water layer thicknesses are initially somewhat different, the thicker water layers would lead to a slower decomposition process of the underlying GHs due to the longer diffusion pathways; this in turn would slow down the increase of water layer thickness with time and eventually result in similar thicknesses (see Figures 5c and 5d). These observations corroborate the central role of melt water acting as a diffusion barrier limiting further decomposition and thus decelerating the decomposition processes. It should be noted that in larger systems than discussed here

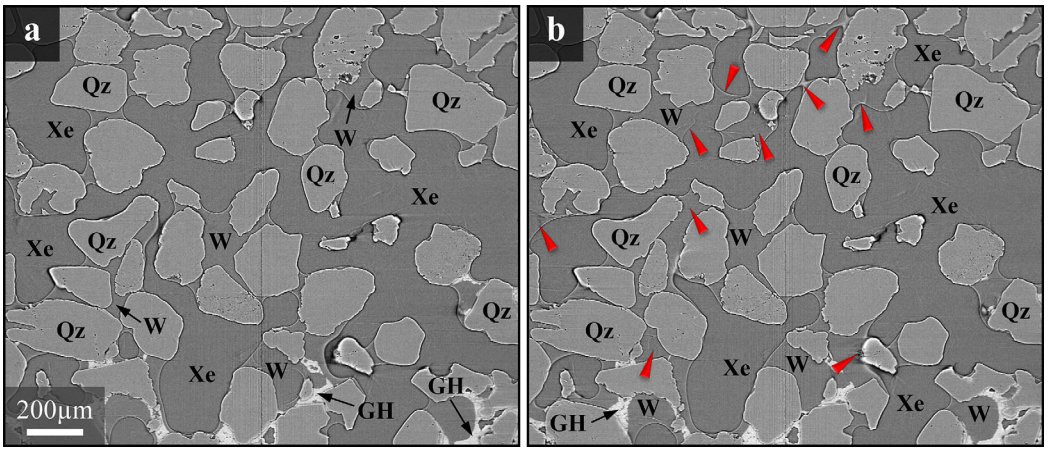

Figure 6. Vertical sections showing water redistributions during decomposition at two time steps. (a) t_R= 20.37 min, (b) t_R=37.87 min. Water (W, gray) appears to uniformly adhere to intergranular spaces at the end of stage II of the decomposition (see a). Most of the residual gas hydrates (GH, white) accumulate at the bottom of the scanned region, enveloped by water. Water patches grow with the decomposition (see red arrows in Figure 6b), rather than a complete rearrangement. Quartz sands (Qz) are shown in light gray, Xe gas (Xe) in gray.

this fundamental aspect of decomposition will be coupled with the heat transfer efficiency which in combination may introduce additional local inhomogeneities.

At the end of stage II melt water is collecting mainly at the contacts between quartz grains and narrower intergranular spaces (see Figure 6a). The surface tensions of hydrophilic quartz sands together with capillary forces likely play an important role in this redistribution. It should be also noted that a gas release during continuous depressurization might have additional influence on the water migration but is not well captured in our few scans. Even more pronounced water displacement can be observed in stage III of hydrate decomposition (see Figure 6b), but instead of a complete rearrangement, existing water patches grow in size in our case as more melt water is supplied. The accumulation of water at pore throats will also strongly decrease the effective gas permeation rates [*Byrnes et al*., 1979; *Thomas and Ward*, 1972], thereby considerably slowing down the hydrate decomposition. This indicates the significance of an effective water removal from decomposing hydrate accumulations for a fast and continuous gas production when expanded to field scale tests in marine sediments through a depressurization method.

3.4. Gas Enrichment of Water

The metastable enrichment of xenon in the melt water during the decomposition (see chapter 3.1) should be seen as a kinetic effect originating in the inability of the system to rapidly move across the solubility gap from very high gas concentration found in GHs to much lower in liquid water. The persistence time of this metastable state is not well known but its sheer presence at the GH interface is likely to have a strong influence on the local decomposition rates. It may also enable local reformation process of GHs in spite of being globally away from the stability conditions [*Chaouachi et al*., 2015]. A high (metastable) gas concentration in water produced from GH decomposition is consistent with earlier observations by optical microscopy which did not show any visible gas bubbles evolving during decomposition as long as the pressure was not completely released [*Tohidi et al*., 2001]. A high concentration of gas molecules in the water at GH interface has been also proposed in the explanation of a long survivability of GH shells surrounding rising bubbles in underwater gas plumes [*Mori*, 1998]. A gradient of gas concentration across the water layer in the direction perpendicular to the interface was suggested as well [*Mori and Mochizuki*, 1997], yet without any indication of the spatial extent into the water column. Our microtomographic data enhanced with the phase retrieval algorithm [*Paganin et al*., 2002] offer a unique access to this missing information in the form of spatial variations of the absorption characteristics on the μm-scale.

By following a change in gray values away from GH interface across the water layer we provide the first experimental evidence of a gas concentration gradient in the direction away from the hydrate surface, shown in Figure 7a. The density contrast of the enriched water decreases initially fast with the increasing distance from the hydrate surface and then levels off at about 12 μm distant from the hydrate-water interface (see Figure 7b); the long distance over which the gray-scale values decrease cannot be ascribed to the

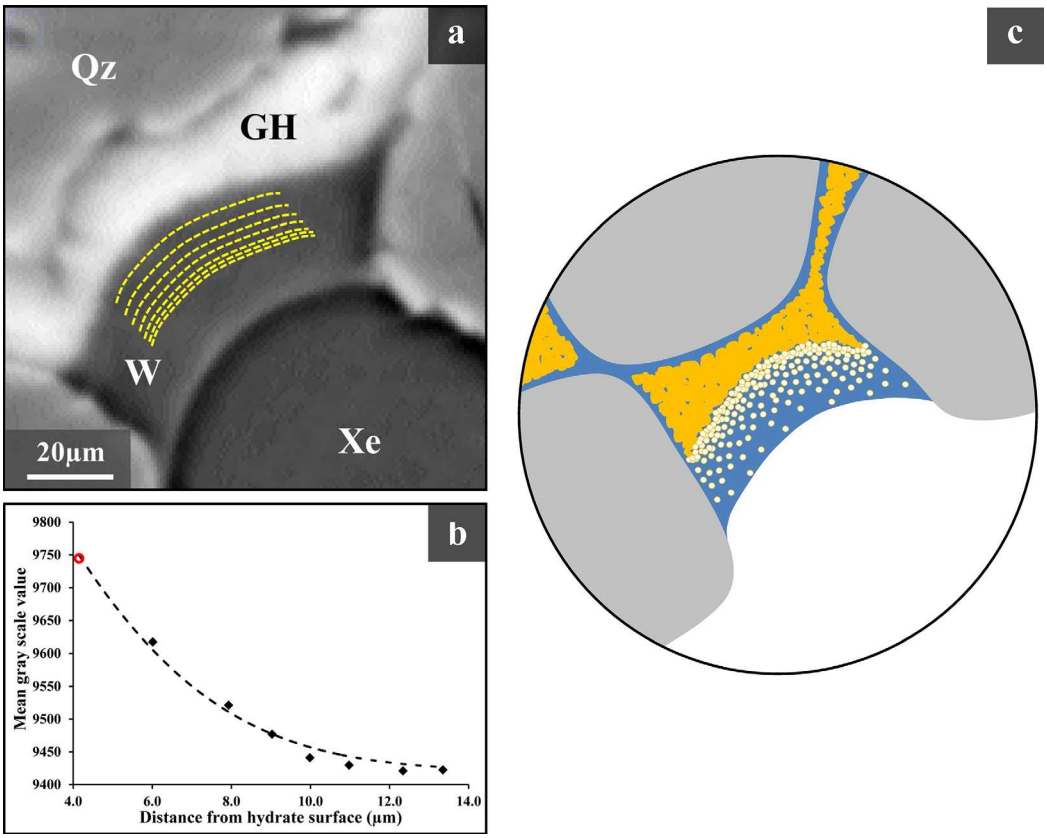

Figure 7. (a) Tomographic image illustrating the meniscus-shaped water layer (W, gray), and the gas concentration gradient across the water layer. To visualize the gradient, the reconstruction has been enhanced with the phase-retrieval algorithm. Gray scales are taken along each yellow dotted line and plotted (see Figure 7b). Quartz sands (Qz) are shown in light gray, Xe gas (Xe) in gray and gas hydrates (GH) in white. (b) Mean gray scale on each line presumably in parallel with the hydrate surface (see a) against its distance from the hydrate surface. The distance is calculated by averaging the distances of 10 points on the line. The trend line is fitted through the diffusion equation based on the Fick's law. The red hollow circle marks a measurement point possibly influenced by the refractory edge enhancement at the GH-water interface and thus not used in the curve fitting. (c) A conceptual model depicting the gas concentration gradient across the water layer resulting from the gas diffusion, with quartz in gray, GHs in yellow, water in blue and gas in white. Hollow spheres are drawn to simulate the accumulation and diffusion of gas molecules produced from hydrate decomposition in the water layer.

refractory edge enhancement at the water-GH boundary that spans over a much shorter distance (see supporting information Figure S3). The change in gray values also cannot be contributed to a density fluctuation in pure substances (measured far from edges) like quartz or water. The standard deviation of the gray scale is fairly insignificant, within ~1%. GH accumulations with a few μm size crystals will be commonly affected by the edge enhancement and thus may display some visible fluctuation in gray values but this fact remains without a consequence for the established concentration gradient in water. The high concentration close to the GH is likely to originate in a dynamic exchange of gas and water existing at the phase boundary, in which gas escaping from destructed cages and recaptured for reformation constantly take place on a μs to s time scale. Such a gas-enriched boundary layer is likely to be present also at the hydrate-water interface at pressure conditions inside the stability field of the hydrates. During the decomposition, a constant depletion of gas molecules *via* diffusion from this oversaturated interface into remote water and eventually into bulk gas will drive the further decomposition of GHs. Since the escape rate of gas molecules is controlled by rather low diffusivity and solubility of Xe in water (see Figure 7c) a well pronounced concentration gradient is established.

The gradient of gas enrichment strongly supports the diffusion limited nature of hydrate decomposition, illustrating the significant role of the water layer next to the decomposing hydrate with a resulting sluggish escape of gas molecules in the course of hydrate decomposition. The high gas activity in the water close to the hydrate will considerably reduce the driving force of decomposition, which is given by the difference in chemical potential [*Kashchiev and Firoozabadi*, 2002]. However, these metastable enrichments will not be

maintained for extended periods of time, even when the system is kept at equilibrium conditions (globally maintained during the tomographic sweeps). Due to the concentration gradient the xenon gas maintained in the water phase will continue to be diffusively transported into the bulk gas phase. Unfortunately, the gray-scale values of tomograms reconstructed from regions-of-interest data cannot be brought on an absolute scale so that absolute values of the concentration gradient cannot be given.

3.5. Gas Hydrate Reformation

Secondary hydrate formation during decomposition (hence at global p-T conditions outside stability field) can be triggered locally by fulfilling a set of conditions that involve the endothermic nature of decomposition [*Sloan and Koh*, 2007], Joule-Thomson effect [*Seol and Myshakin*, 2011], local repressurization resulting from capillary pressure [*Henry et al*., 1999], preexisting GH surface (no nucleation barrier) and anomalous enrichment of xenon in water sufficiently large to initiate the reaction. This phenomenon would possibly result in temporal, local plugging problems of gas and water transportation and thus a local pressure rise [*Lee et al*., 2010], which may have a detrimental impact for a sustainable gas recovery [*Seol and Myshakin*, 2011] as well as on the sediment stability. Results from large-scale numerical simulations have depicted the reformation of GHs during depressurization by a substantial increase of hydrate saturation remote from the decomposing front [*Moridis and Reagan*, 2007]. Likewise, with the help of distributed pressure sensors in the vessel, hydrate regeneration during decomposition was also suggested by a local pressure increase [*Lee et al*., 2010], yet without microstructural evidence.

Our findings clearly demonstrate that localized hydrate reformation from melt water (see chapter 3.4) is possible (see Figure 8) albeit only within stage I of decomposition, where the reaction is very rapid and the high saturation of GHs may cause local repressurization. The reformation occurs preferentially at the existing hydrate surface wherever favorable local p-T-x conditions are found; these are controlled by a spatial inhomogeneous heat distribution due to the endothermic character of hydrate decomposition, as well as a local pressure increase arising from the low permeability and capillary forces. Consequently, reformed hydrates are frequently found to replace gas pockets residing in hydrate patches and fill narrow gaps between quartz crystals (see Figure 8). Moreover, our tomographic images indicate that regions with high hydrate saturations are more likely to facilitate a secondary hydrate formation. Further decomposition stages with slower decomposition rates and lower hydrate saturations do not show any substantial reformation. Mitigation of possible plugging problems deriving from the local reformation effect during depressurization-induced gas production may require an effective management of the reaction rate, such as keeping a smaller pressure difference between internal-equilibrium and outlet during depressurization [*Lee et al*., 2010].

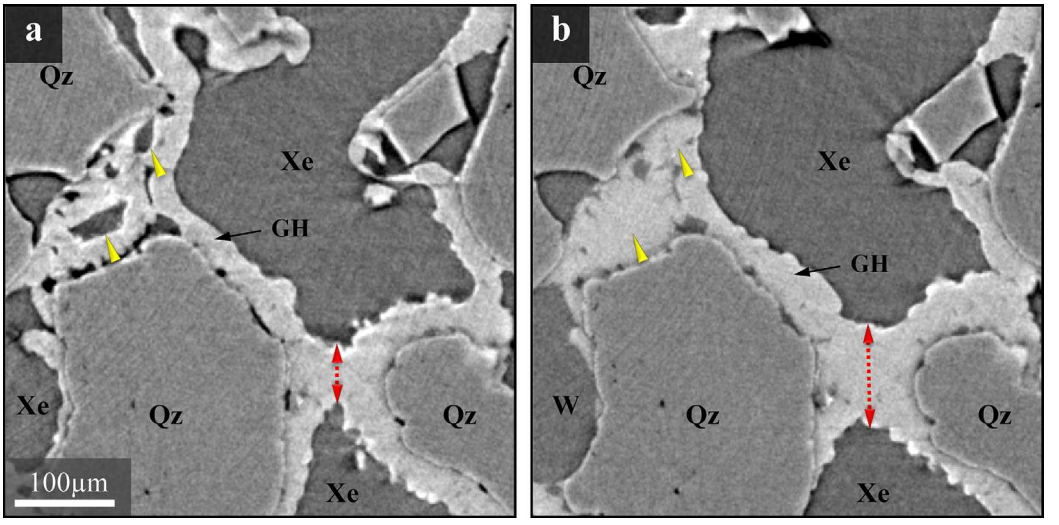

Figure 8. Secondary hydrate formation during decomposition. (a) Full formation, (b) t_R=10s. Gas hydrate (GH, white) reformation is taking place *via* a growth at the existing hydrate surface toward gas phase (red arrows and lines). Reformed hydrates can also replace gas pockets in hydrate patches (yellow arrows). Quartz sands (Qz) are shown in light gray, Xe gas (Xe) and water (W) in gray.

4. Discussion and Conclusions

4.1. Comparison of Xenon and Methane Case

Xenon and methane as well as their corresponding hydrates display a number of similar physical properties allowing for a convenient substitution of one gas with another one [*Chaouachi et al*., 2015]. At the same time Xe offers greatly enhanced absorption of X-rays (without which the observations on the concentration gradients in the water film could hardly have been made) and alleviates a number of serious risks related to the operations with potentially explosive gas under pressure (which is a critical point at large scale research facilities). However, it should be kept in mind that the substitution is not perfect in every respect even if far more accurate than in case of e.g., THF hydrate. Xe being heavier than methane displays greater solubility in water; a factor of 3.86 at 273.15 K [*Haynes*, 2014]. This might have helped somewhat the metastable enrichments of Xe gas in water during decomposition. Methane, on the other hand, can diffuse about 33% faster than xenon in water at 283.15 K [*Haynes*, 2014], which may somewhat enhance the diffusion limited decomposition when extrapolated to methane case. Since the decomposition behavior is largely governed by the supersaturation of melt water in the vicinity to GH surface, the differences in the solubility and diffusion coefficients will influence the shape of the compositional gradient, but the phenomena are expected to be qualitatively the same. Indeed, molecular dynamics and electron microscopic work on methane hydrate decomposition have repeatedly observed the formation of nano- to micro- scale gas bubbles which may be the vesicles for the metastable enrichments in the liquid state [*Bagherzadeh et al*., 2013, 2015; *Uchida et al*., 2016a, 2016b]. Persistence and size of such nano-bubbles is likely to be somewhat different for Xe and CH_4 systems.

4.2. Decomposition and Mechanical Stability

The decomposition of GHs by depressurization does not lead to a sudden disintegration of all GH crystals in the volume. On the contrary, characteristically the initial melting is triggered at hydrate surfaces with crystals protruding into the gas phase. Due to a larger specific surface area and hence very unfavorable surface free energy of such interface the initial decomposition smoothens the GH surface through the melting and partial reformation (see Figures 9a and 9b). The melting of GH is a classic example of the first order transition where thermodynamically unstable clathrate crystals can coexist for prolonged time with the decomposition products. With the continuous depletion of gas from the melt water the reformation becomes increasingly less likely and water molecules accumulate at the retreating hydrate surface thus forming a gradually thickening diffusion barrier. The hydrate dissolution front ultimately mirrors the shape of the neighboring gas-water interface, resulting from the gas diffusion mechanism (see Figure 9c). GH patches continue to shrink with external hydrate surface ablating toward narrow grain contacts in the course of decomposition. Notably the interfacial water film at GH-quartz interface retains the anomalously high gas saturation throughout the dissolution process (due to limited out-diffusion gateways) as it can be recognized by sharp tips of wedge-shaped hydrate patches in the interstices between grain surfaces (see Figure 9d) that hold grains in place *via* a cushion of water layer residing between them [*Chaouachi et al*., 2015]. Such a shape is likely to considerably restrain the rolling and shear motion of the grains which helps to maintain the small-strain stiffness and shear strength of the sediments during decomposition. The hydrate assemblies remain topologically intact until the hydrate spacers finally dissolve leading to a drop in failure

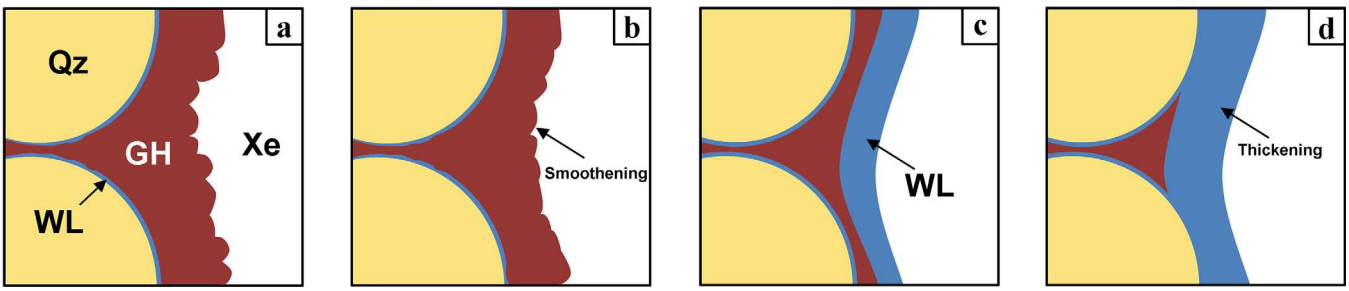

Figure 9. A conceptual model of hydrate decomposition. GHs (dark red) prefer to form close to the quartz sand (Qz, light yellow) surface with a thin water layer (WL, blue) between them. A coarse hydrate surface with single crystals protruding into the xenon gas (Xe, white) phase will preferentially decompose to smoothen the GH-gas interface; A water layer subsequently accumulates at the hydrate surface and then thickens with the decomposition. GHs gradually shrink toward narrow grain contacts and frequently form a wedge-shaped hydrate patch in the interstices between grain surfaces, which will considerably help to maintain the mechanical strength of the sediments during decomposition.

strength of the sediments [*Song et al*., 2014]. This regime established in our observations would provide insights into the mechanical stability of marine sediments during a suggested depressurization-induced gas production. Please note, hydrate decomposition induced by other approaches, like thermal stimulation, may yield different hydrate morphologies, thus displaying different mechanical properties [*Priest et al*., 2011]. Moreover, the decomposition couples with a gas production which induces a remarkable increase of the pore pressure, especially within the low permeability regions [*Max*, 2003; *Winters et al*., 2007]. This would intensify the total stress on the sediments, thereby likely triggering a failure as the decline of the sediment mechanical strength; at particular risk is the hydrate reservoir in shallow soils, where a sufficient confining pressure is not available, and thus is more prone to failure [*Song et al*., 2014]. Therefore, the weakening of sediment strength with hydrate decomposition is possibly responsible for the slope failures [*Max*, 2003], borehole instabilities [*Nimblett et al*., 2005], as well as sand problems during exploitation [*Yamamoto et al*., 2014].

4.3. Mass Transfer Limitations of the Decomposition Process

Our initial gas-rich system with their - in the course of decomposition - evolving water layers and resulting gas-water interfaces may not be archetypical for all natural environments of hydrate accumulations under the seafloor. Yet the situations developing during decomposition with a water layer acting as a diffusive barrier are likely operational in all sediments, also initially fully water-saturated ones after the appearance of a bulk gas phase. In addition, our *in-situ* results on the gas concentration gradient across liquid water provide strong evidences on the mass transfer limitation during decomposition. As a side remark, the mass transfer of gas in water and the elucidated possible transport mechanisms and supersaturation allow a "fresh look" on the formation process, and possibly a gas exchange reaction as well. The mass transfer problems have been encountered in previous investigations on the intrinsic kinetic model for hydrate growth, in which a stirred tank reactor was employed to accelerate the transformation [*Englezos et al*., 1987a, 1987b]; on this basis, a rate-determining step of the gas transport into liquid water phase was assumed to simplify the model [*Skovborg and Rasmussen*, 1994]. The large overpressure needed for hydrate formation in pure liquid systems is likely also a consequence of this mass transfer limitation [*Osegovic et al*., 2007]. Our findings on a concentration gradient of metastably enriched gas in the liquid phase during decomposition imply a potentially positive effect of this scenario on the enhancement of hydrate reformation, despite the mass transfer barrier; of particular interest is its application in hydrate-based techniques like natural gas storage and transportation, where a faster and more complete transformation of water into hydrates can likely be expected and were in fact repeatedly observed [*Ohmura et al*., 2003; *Wu and Zhang*, 2010].

4.4. Permeation of the Sedimentary Matrix

At last, we want to address the implications of our work on the permeation properties of hydrate-bearing sediments, which vary considerably with differing microstructural growth habit of hydrates in pore spaces [*Dai et al*., 2012; *Kleinberg et al*., 2003]; hence, the morphological evolution of hydrate patch during decomposition will also significantly govern the permeability, and subsequently the gas production behavior. An effective permeability higher than the threshold value is necessary for a feasible commercial gas recovery from marine hydrate reservoirs through depressurization [*Konno et al*., 2010b]. Permeability is calculated to be always higher for hydrates forming grain-coating patterns than for those displaying pore-filling at specific hydrate saturations [*Dai et al*., 2012; *Kumar et al*., 2010]. Our observations on hydrates accumulating close to grain surfaces with a water film residing between them are supposed to result in an intermediate permeability value in comparison with the two patterns above. Furthermore, the revealed decomposition regime with hydrate surfaces exposed to pore gas ablating toward the quartz grain surface, rather than evolving at the quartz-hydrate interface, will also have positive effects on the further improvements of the sediment permeability during decomposition; because the latter scenario will eventually result in a pore-filling pattern of hydrates in pores. As an example gas venting and water flux *via* the pore network was studied for cold-vent shallow GHs at Cascadia margin with implications for their formation age [*Cao et al*., 2013]; the transport could take place within the sediments as well as along the liquid layers at the hydrate-grain interfaces.

This work is based on the observations in an mm-scale-diameter pressure vessel in order to get access to the microstructural evolutions of hydrate decomposition; still, the scenarios established likely also provide some insight into the microstructural changes of hydrate decomposition at larger scales up to field tests.

Certainly, the decomposition process here is completed in a time span of tens of minutes, which is not comparable to that of a field test with days or even years of gas recovery. However, the evolution of microstructural features, the location of preferential decomposition sites or the out-diffusion barrier and rate-limiting role of water layers between the decomposing clathrates and the gas phase developed in our study, will have implications for the hydrate decomposition behavior in long-term gas production trials. Undoubtedly, the latent heat in the reservoirs, heat supply from surrounding environments as well as mass transfer issues in tests with increased time- and space- scales will bring about even more pronounced inhomogeneities of hydrate decomposition and gas/water rearrangements; this is unfortunately beyond the scale of our experiment and will need considerable modeling efforts. Our observations on a gas-rich system bear some generalities of the decomposition behavior and could guide to model and predict also what happens in nature scale geological settings during a depressurization-induced decomposition.

Acknowledgments

We acknowledge the Paul Scherrer Institut, Villigen, Switzerland for providing synchrotron radiation beamtime at the TOMCAT beamline of the SLS. We are very grateful to Frieder Enzmann (University of Mainz) for his competent help with data reduction and analysis. We also thank Kathleen Sell, Jens-Oliver Schwarz, Martin Wolf and Faisal Khan (all University of Mainz) for their valuable help during the experiments. The pressure cell was designed and constructed by Ulf Kahmann and Heiner Bartels (both University of Göttingen). The financial support from the Deutsche Forschungsgemeinschaft (DFG Grant Ku 920/18 and Ke 508/20) as well as the BMBF in the framework of the SUGAR-III program (grant 03G0856B) is gratefully acknowledged. The financial support to Lei Yang from the China Scholarship Council is also acknowledged. The tomography data used as basis of our work (~5.4 TB for the reconstructed data, an additional ~1.2 TB for the Paganin-treated data) can be made available upon request to Werner F. Kuhs (e-mail: wkuhs1@gwdg.de).

References

Abràmoff, M. D., P. J. Magalhães, and S. J. Ram (2004), Image processing with ImageJ, *Biophotonics Int.*, *11*(7), 36–42.

Anderson, B. J., et al. (2011), Regional long-term production modeling from a single well test, Mount Elbert Gas Hydrate Stratigraphic Test Well, Alaska North Slope, *Mar. Pet. Geol.*, *28*(2), 493–501.

Bagherzadeh, S. A., P. Englezos, S. Alavi, and J. A. Ripmeester (2012), Molecular modeling of the dissociation of methane hydrate in contact with a silica surface, *J. Phys. Chem. B*, *116*(10), 3188–3197.

Bagherzadeh, S. A., S. Alavi, J. A. Ripmeester, and P. Englezos (2013), Evolution of methane during gas hydrate dissociation, *Fluid Phase Equilibria*, *358*, 114–120.

Bagherzadeh, S. A., S. Alavi, J. Ripmeester, and P. Englezos (2015), Formation of methane nano-bubbles during hydrate decomposition and their effect on hydrate growth, *J. Chem. Phys.*, *142*(21), 214701.

Bai, D., G. Chen, X. Zhang, and W. Wang (2011), Microsecond molecular dynamics simulations of the kinetic pathways of gas hydrate formation from solid surfaces, *Langmuir*, *27*, 5961–5967.

Baldwin, B. A., A. Moradi-Araghi, and J. C. Stevens (2003), Monitoring hydrate formation and dissociation in sandstone and bulk with magnetic resonance imaging, *Magn. Reson. Imaging*, *21*(9), 1061–1069.

Bonnefoy, O., F. Gruy, and J. M. Herri (2005), Van der Waals interactions in systems involving gas hydrates, *Fluid Phase Equilibria*, *231*(2), 176–187.

Byrnes, A. P., K. Sampath, and P. Randolph (1979), Effect of pressure and water saturation on permeability of western tight sandstones, paper presented at Fifth Annual DOE Symposium on Enhanced Oil and Gas Recovery and Improved Drilling Technology, U.S. Department of Energy, Tulsa, Okla.

Cao, Y., D. Chen, and L. M. Cathles (2013), A kinetic model for the methane hydrate precipitated from venting gas at cold seep sites at Hydrate Ridge, Cascadia margin, Oregon, *J. Geophys. Res. Solid Earth*, *118*, 4669–4681, doi:10.1002/jgrb.50351.

Chandler, D. (2005), Interfaces and the driving force of hydrophobic assembly, *Nature*, *437*(7059), 640–647.

Chaouachi, M., A. Falenty, K. Sell, F. Enzmann, M. Kersten, D. Haberthür, and W. Kuhs (2015), Microstructural evolution of gas hydrates in sedimentary matrices observed with synchrotron X-ray computed tomographic microscopy, *Geochem. Geophys. Geosyst.*, *16*, 1711–1722, doi:10.1002/2015GC005811.

Chong, Z. R., S. H. B. Yang, P. Babu, P. Linga, and X.-S. Li (2016), Review of natural gas hydrates as an energy resource: Prospects and challenges, *Appl. Energy*, *162*, 1633–1652.

Chuvilin, E. M., V. A. Istomin, and S. S. Safonov (2011), Residual nonclathrated water in sediments in equilibrium with gas hydrate Comparison with unfrozen water, *Cold Reg. Sci. Technol.*, *68*(1–2), 68–73.

Collett, T. (1999), Detailed evaluation of gas hydrate reservoir properties using JAPEX/JNOC/GSC Mallik 2L-38 gas hydrate research well downhole well-log displays, *Bull. Geol. Surv. Can.*, *544*, 295–311.

Dai, S., J. C. Santamarina, W. F. Waite, and T. J. Kneafsey (2012), Hydrate morphology: Physical properties of sands with patchy hydrate saturation, *J. Geophys. Res.*, *117*, B11205, doi:10.1029/2012JB009667.

Dillon, W. P., J. W. Nealon, M. H. Taylor, M. W. Lee, R. M. Drury, and C. H. Anton (2001), Seafloor collapse and methane venting associated with gas hydrate on the blake ridge: causes and implications to seafloor stability and methanerelease, in *Natural Gas Hydrates: Occurrence, Distribution, and Detection*, edited by C. K. Paull and W. P. Dillon, pp. 211–233, AGU, Washington, D. C.

Englezos, P., N. Kalogerakis, P. D. Dholabhai, and P. R. Bishnoi (1987a), Kinetics of gas hydrate formation from mixtures of methane and ethane, *Chem. Eng. Sci.*, *42*(11), 2659–2666.

Englezos, P., N. Kalogerakis, P. Dholabhai, and P. Bishnoi (1987b), Kinetics of formation of methane and ethane gas hydrates, *Chem. Eng. Sci.*, *42*(11), 2647–2658.

Falenty, A., A. N. Salamatin, and W. F. Kuhs (2013), Kinetics of CO_2-hydrate formation from ice powders: Data summary and modeling extended to low temperatures, *J. Phys. Chem. C*, *117*(16), 8443–8457.

Falenty, A., W. F. Kuhs, M. Glockzin, and G. Rehder (2014), "Self-Preservation" of CH_4 hydrates for gas transport technology: Pressure-temperature dependence and ice microstructures, *Energ Fuel*, *28*(10), 6275–6283.

Falenty, A., M. Chaouachi, S. H. Neher, K. Sell, J.-O. Schwarz, M. Wolf, F. Enzmann, M. Kersten, D. Haberthur, and W. F. Kuhs (2015), Stop-and-go in situ tomography of dynamic processes - gas hydrate formation in sedimentary matrices, *Acta Crystallogr. Sect. A Found. Crystallogr.*, *71*(a1), s154.

Gao, S., W. House, and W. G. Chapman (2005), NMR/MRI Study of clathrate hydrate mechanisms, *J. Phys. Chem. B*, *109*(41), 19090–19093.

Haligva, C., P. Linga, J. Ripmeester, and P. Englezos (2010), Recovery of methane from a variable-volume bed of silica sand/hydrate by depressurization, *Energ Fuel*, *24*(5), 2947–2955.

Haynes, W. M. (2014), *CRC Handbook of Chemistry and Physics*, CRC Press, Boca Raton, Fla.

Henke, B. L., E. M. Gullikson, and J. C. Davis (1993), X-ray interactions: Photoabsorption, scattering, transmission, and reflection at E = 50-30,000 eV, Z = 1-92, *At. Data Nucl. Data Tables*, *54*(2), 181–342.

Henry, P., M. Thomas, and M. B. Clennell (1999), Formation of natural gas hydrates in marine sediments 2. Thermodynamic calculations of stability conditions in porous sediments, *J. Geophys. Res.*, *104*(B10), 23005–23022.

Hirata, A., and Y. H. Mori (1998), How liquids wet clathrate hydrates: Some macroscopic observations, *Chem. Eng. Sci.*, *53*(14), 2641–2643.
Hyndman, R. D., T. Yuan, and K. Moran (1999), The concentration of deep sea gas hydrates from downhole electrical resistivity logs and laboratory data, *Earth Planet. Sci. Lett.*, *172*(1–2), 167–177.
Ji, C., G. Ahmadi, and D. Smith (2001), Natural gas production from hydrate decomposition by depressurization, *Chem. Eng. Sci.*, *56*(20), 5801–5814.
Kashchiev, D., and A. Firoozabadi (2002), Driving force for crystallization of gas hydrates, *J. Cryst. Growth*, *241*(1–2), 220–230.
Katsuki, D., R. Ohmura, T. Ebinuma, and H. Narita (2008), Visual observation of dissociation of methane hydrate crystals in a glass micro model: Production and transfer of methane, *J. Appl. Phys.*, *104*(8), 083514.
Kim, H. C., P. R. Bishnoi, R. A. Heidemann, and S. S. H. Rizvi (1987), Kinetics of methane hydrate decomposition, *Chem. Eng. Sci.*, *42*(7), 1645–1653.
Klapp, S. A., F. Enzmann, P. Walz, T. Huthwelker, J. R. Tuckermann, J.-O. Schwarz, T. Pape, E. T. Peltzer, R. Mokso, and D. Wangner (2012), Microstructure characteristics during hydrate formation and dissociation revealed by X-ray tomographic microscopy, *Geo Mar. Lett.*, *32*(5-6), 555–562.
Kleinberg, R. L., C. Flaum, D. D. Griffin, P. G. Brewer, G. E. Malby, E. T. Peltzer, and J. P. Yesinowski (2003), Deep sea NMR: Methane hydrate growth habit in porous media and its relationship to hydraulic permeability, deposit accumulation, and submarine slope stability, *J. Geophys. Res.*, *108*(B10), 2508, doi:10.1029/2003JB002389.
Kneafsey, T., L. Tomutsa, G. Moridis, Y. Seol, B. Freifeld, C. Taylor, and A. Gupta (2007), Methane hydrate formation and dissociation in a partially saturated core-scale sand sample, *J. Pet. Sci. Eng.*, *56*(1), 108–126.
Koh, C. A., E. D. Sloan, and A. Sum (2010), *Natural Gas Hydrates in Flow Assurance*, Gulf Prof. Publ., Houston, Tex.
Komai, T., S.-P. Kang, J.-H. Yoon, Y. Yamamoto, T. Kawamura, and M. Ohtake (2004), In Situ Raman Spectroscopy investigation of the dissociation of methane hydrate at temperatures just below the ice point, *J. Phys. Chem. B*, *108*(23), 8062–8068.
Konno, Y., H. Oyama, J. Nagao, Y. Masuda, and M. Kurihara (2010a), Numerical analysis of the dissociation experiment of naturally occurring gas hydrate in sediment cores obtained at the eastern Nankai Trough, Japan, *Energ Fuel*, *24*(12), 6353–6358.
Konno, Y., Y. Masuda, Y. Hariguchi, M. Kurihara, and H. Ouchi (2010b), Key factors for depressurization-induced gas production from oceanic methane hydrates, *Energ Fuel*, *24*(3), 1736–1744.
Kono, H., S. Narasimhan, F. Song, and D. Smith (2002), Synthesis of methane gas hydrate in porous sediments and its dissociation by depressurizing, *Powder Technol.*, *122*(2-3), 239–246.
Krey, V., J. G. Canadell, N. Nakicenovic, Y. Abe, H. Andruleit, D. Archer, A. Grubler, N. T. Hamilton, A. Johnson, and V. Kostov (2009), Gas hydrates: Entrance to a methane age or climate threat?, *Environ. Res. Lett.*, *4*(3), 034007.
Kuhs, W. F., A. Klapproth, F. Gotthardt, K. Techmer, and T. Heinrichs (2000), The formation of meso- and macroporous gas hydrates, *Geophys. Res. Lett.*, *27*(18), 2929–2932.
Kumar, A., B. Maini, P. R. Bishnoi, M. Clarke, O. Zatsepina, and S. Srinivasan (2010), Experimental determination of permeability in the presence of hydrates and its effect on the dissociation characteristics of gas hydrates in porous media, *J. Pet. Sci. Eng.*, *70*(1–2), 114–122.
Lee, J., S. Park, and W. Sung (2010), An experimental study on the productivity of dissociated gas from gas hydrate by depressurization scheme, *Energy Convers. Manage.*, *51*(12), 2510–2515.
Li, X.-S., Y. Zhang, G. Li, Z.-Y. Chen, and H.-J. Wu (2011), Experimental investigation into the production behavior of methane hydrate in porous sediment by depressurization with a novel three-dimensional cubic hydrate simulator, *Energ Fuel*, *25*(10), 4497–4505.
Li, X.-S., Y. Wang, G. Li, and Y. Zhang (2012a), Experimental investigations into gas production behaviors from methane hydrate with different methods in a cubic hydrate simulator, *Energ Fuel*, *26*(2), 1124–1134.
Li, X.-S., B. Yang, Y. Zhang, G. Li, L.-P. Duan, Y. Wang, Z.-Y. Chen, N.-S. Huang, and H.-J. Wu (2012b), Experimental investigation into gas production from methane hydrate in sediment by depressurization in a novel pilot-scale hydrate simulator, *Appl. Energy*, *93*, 722–732.
Liang, S., D. Rozmanov, and P. G. Kusalik. (2011), Crystal growth simulations of methane hydrates in the presence of silica surfaces, *Phys. Chem. Chem. Phys.*, *13*(44), 19,856–19,864.
Linga, P., C. Haligva, S. Nam, J. Ripmeester, and P. Englezos (2009), Recovery of methane from hydrate formed in a variable volume bed of silica sand particles, *Energy Fuel*, *23*(11), 5508–5516.
Liu, C., H. Lu, Y. Ye, J. Ripmeester, and X. Zhang (2008), Raman spectroscopic observations on the structural characteristics and dissociation behavior of methane hydrate synthesized in silica sands with various sizes, *Energy Fuel*, *22*(6), 3986–3988.
Marone, F., and M. Stampanoni (2012), Regridding reconstruction algorithm for real-time tomographic imaging, *J. Synchrotron Radiat.*, *19*(6), 1029–1037.
Max, M. D. (2003), *Natural Gas Hydrate in Oceanic and Permafrost Environments*, Springer.
Mori, Y. H. (1998), Clathrate hydrate formation at the interface between liquid CO_2 and water phases-a review of rival models characterizing "hydrate films," *Energy Convers. Manage.*, *39*(15), 1537–1557.
Mori, Y. H., and T. Mochizuki (1997), Mass transport across clathrate hydrate films-a capillary permeation model, *Chem. Eng. Sci.*, *52*(20), 3613–3616.
Moridis, G. (2004), Numerical studies of gas production from class 2 and class 3 hydrate accumulations at the Mallik Site, Mackenzie Delta, Canada, *SPE Reservoir Eval. Eng.*, *7*(03), 175–183.
Moridis, G., and M. Reagan (2007), Strategies for gas production from oceanic Class 3 hydrate accumulations, paper presented at Offshore Technology Conference, Houston, Tex.
Moridis, G., T. Collett, S. Dallimore, T. Satoh, S. Hancock, and B. Weatherill (2004), Numerical studies of gas production from several CH_4 hydrate zones at the Mallik site, Mackenzie Delta, Canada, *J. Pet. Sci. Eng.*, *43*(3-4), 219–238.
Moridis, G. J. (2011), Challenges, uncertainties and issues facing gas production from gas hydrate deposits, *SPE Reservoir Eval. Eng.*, *14*(1), 76–112.
Murshed, M. M., S. A. Klapp, F. Enzmann, T. Szeder, T. Huthwelker, M. Stampanoni, F. Marone, C. Hintermüller, G. Bohrmann, and W. F. Kuhs (2008), Natural gas hydrate investigations by synchrotron radiation X-ray cryo-tomographic microscopy (SRXCTM), *Geophys. Res. Lett.*, *35*, L23612, doi:10.1029/2008GL035460.
Nimblett, J., R. Shipp, and F. Strijbos (2005), Gas hydrate as a drilling hazard: Examples from global deepwater settings, paper presented at Offshore Technology Conference, American Association of Petroleum Geologists (AAPG), Houston, Tex.
Ohmura, R., M. Ogawa, K. Yasuoka, and Y. H. Mori (2003), Statistical study of clathrate-hydrate nucleation in a water/hydrochlorofluorocarbon system: Search for the nature of the "memory effect," *J. Phys. Chem. B*, *107*(22), 5289–5293.
Osegovic, J. P., S. R. Tatro, S. A. Holman, A. L. Ames, and M. D. Max (2007), Growth kinetics of ethane hydrate from a seawater solution at an ethane gas interface, *J. Pet. Sci. Eng.*, *56*(1), 42–46.
Paganin, D., S. Mayo, T. E. Gureyev, P. R. Miller, and S. W. Wilkins (2002), Simultaneous phase and amplitude extraction from a single defocused image of a homogeneous object, *J. Microsc.*, *206*(1), 33–40.

Pauli, C., W. Ussler III, and W. Dillon (2003), Potential role of gas hydrate decomposition in generating submarine slope failures, in *Natural Gas Hydrate*, edited by M. Max, pp. 149–156, Springer Netherlands, Dordrecht, Netherlands.

Pauli, C. K., W. Ussler III, and W. P. Dillon (2000), Potential role of gas hydrate decomposition in generating submarine slope failures, in *Natural Gas Hydrate*, edited by Michael D. Max, pp. 149–156, Springer, Berlin, Germany.

Poirier, J.-P. (2000), *Introduction to the Physics of the Earth's Interior*, Cambridge Univ. Press, Cambridge, England.

Priest, J., A. Sultaniya, and C. Clayton (2011), Impact of hydrate formation and dissociation on the stiffness of a sand, paper presented at Proceedings of the 7th international conference on gas hydrates (ICGH 2011), Heriot-Watt University, Edinburgh, U. K.

Promentilla, M. A. B., and T. Sugiyama (2010), X-ray microtomography of mortars exposed to freezing-thawing action, *J. Adv. Concrete Technol.*, *8*(2), 97–111.

Salamatin, A. N., A. Falenty, T. C. Hansen, and W. F. Kuhs (2015), Guest migration revealed in CO_2 clathrate hydrates, *Energy Fuel*, *29*(9), 5681–5691.

Sell, K., E. H. Saenger, A. Falenty, M. Chaouachi, D. Haberthür, F. Enzmann, W. F. Kuhs, and M. Kersten (2016), On the path to the digital rock physics of gas hydrate-bearing sediments – processing of in situ synchrotron-tomography data, *Solid Earth*, *7*(4), 1243–1258.

Seol, Y., and E. Myshakin (2011), Experimental and numerical observations of hydrate reformation during depressurization in a core-scale reactor, *Energy Fuel*, *25*(3), 1099–1110.

Shulakova, V., M. Pervukhina, T. M. Müller, M. Lebedev, S. Mayo, S. Schmid, P. Golodoniuc, O. B. De Paula, M. B. Clennell, and B. Gurevich (2013), Computational elastic up-scaling of sandstone on the basis of X-ray micro-tomographic images, *Geophys. Prospect.*, *61*(2), 287–301.

Skovborg, P., and P. Rasmussen (1994), A mass transport limited model for the growth of methane and ethane gas hydrates, *Chem. Eng. Sci.*, *49*(8), 1131–1143.

Sloan, E. D., and C. Koh (2007), *Clathrate Hydrates of Natural Gases*, 3rd ed., CRC Press, Boca Raton, Fla.

Smirnov, G. S., and V. V. Stegailov (2012), Melting and superheating of sI methane hydrate: Molecular dynamics study, *J. Chem. Phys.*, *136*(4), 044523.

Song, Y., Y. Zhu, W. Liu, J. Zhao, Y. Li, Y. Chen, Z. Shen, Y. Lu, and C. Ji (2014), Experimental research on the mechanical properties of methane hydrate-bearing sediments during hydrate dissociation, *Mar. Pet. Geol.*, *51*, 70–78.

Stampanoni, M., et al. (2006), Trends in synchrotron-based tomographic imaging: The SLS experience, paper presented at SPIE Proceedings, International Society for Optics and Photonics, Orlando, Fla.

Sun, X., and K. Mohanty (2006), Kinetic simulation of methane hydrate formation and dissociation in porous media, *Chem. Eng. Sci.*, *61*(11), 3476–3495.

Tang, L.-G., X.-S. Li, Z.-P. Feng, G. Li, and S.-S. Fan (2007), Control mechanisms for gas hydrate production by depressurization in different scale hydrate reservoirs, *Energy Fuel*, *21*(1), 227–233.

Thomas, R. D., and D. C. Ward (1972), Effect of overburden pressure and water saturation on gas permeability of tight sandstone cores, *JPT J. Pet. Technol.*, *24*(02), 120–124.

Tohidi, B., R. Burgass, A. Danesh, K. Østergaard, and A. Todd (2000), Improving the accuracy of gas hydrate dissociation point measurements, *Ann. N. Y. Acad. Sci.*, *912*(1), 924–931.

Tohidi, B., R. Anderson, M. B. Clennell, R. W. Burgass, and A. B. Biderkab (2001), Visual observation of gas-hydrate formation and dissociation in synthetic porous media by means of glass micromodels, *Geology*, *29*(9), 867–870.

Tsimpanogiannis, I., and P. Lichtner (2007), Parametric study of methane hydrate dissociation in oceanic sediments driven by thermal stimulation, *J. Pet. Sci. Eng.*, *56*(1), 165–175.

Uchida, T., K. Yamazaki, and K. Gohara (2016a), Generation of micro-and nano-bubbles in water by dissociation of gas hydrates, *Korean J. Chem. Eng.*, *33*(5), 1749–1755.

Uchida, T., S. Liu, M. Enari, S. Oshita, K. Yamazaki, and K. Gohara (2016b), Effect of NaCl on the lifetime of micro-and nanobubbles, *Nanomaterials*, *6*(2), 31.

Waite, W. F., T. J. Kneafsey, W. J. Winters, and D. Mason (2008), Physical property changes in hydrate-bearing sediment due to depressurization and subsequent repressurization, *J. Geophys. Res.*, *113*, B07102, doi:10.1029/2007JB005351.

Wang, Y., J.-C. Feng, X.-S. Li, Y. Zhang, and G. Li (2016), Large scale experimental evaluation to methane hydrate dissociation below quadruple point in sandy sediment, *Appl. Energy*, *162*, 372–381.

Winters, W. J., W. F. Waite, D. Mason, L. Gilbert, and I. Pecher (2007), Methane gas hydrate effect on sediment acoustic and strength properties, *J. Pet. Sci. Eng.*, *56*(1), 127–135.

Wu, Q., and B. Zhang (2010), Memory effect on the pressure-temperature condition and induction time of gas hydrate nucleation, *J. Nat. Gas Chem.*, *19*(4), 446–451.

Xu, W., and C. Ruppel (1999), Predicting the occurrence, distribution, and evolution of methane gas hydrate in porous marine sediments, *J. Geophys. Res.*, *104*(B3), 5081–5095.

Yagasaki, T., M. Matsumoto, Y. Andoh, S. Okazaki, and H. Tanaka (2014), Effect of bubble formation on the dissociation of methane hydrate in water: A molecular dynamics study, *J. Phys. Chem. B*, *118*(7), 1900–1906.

Yamamoto, K., Y. Terao, T. Fujii, T. Ikawa, M. Seki, M. Matsuzawa, and T. Kanno (2014), Operational overview of the first offshore production test of methane hydrates in the Eastern Nankai Trough, paper presented at Offshore Technology Conference, American Association of Petroleum Geologists (AAPG), Houston, Tex.

Ye, Y., and C. Liu (2012), *Natural Gas Hydrates: Experimental Techniques and Their Applications*, Springer Sci. & Business Media, Berlin, Germany.

Zhao, J., Z. Zhu, Y. Song, W. Liu, Y. Zhang, and D. Wang (2015), Analyzing the process of gas production for natural gas hydrate using depressurization, *Appl. Energy*, *142*, 125–134.